

REPORT DOCUMENTATION PAGE		READ INSTRUCTIONS BEFORE COMPLETING FORM
1. REPORT NUMBER TR 7299	2. GOVT ACCESSION NO.	3. RECIPIENT'S CATALOG NUMBER
4. TITLE (and Subtitle) THEORETICAL AND EXPERIMENTAL COMPARISONS OF NEARFIELD ELECTROGALVANIC FIELDS DUE TO NON-LINEAR POLARIZATION LAYERS		5. TYPE OF REPORT & PERIOD COVERED Interim Report
		6. PERFORMING ORG. REPORT NUMBER TR 7299
7. AUTHOR(s) Rolf G. Kasper		8. CONTRACT OR GRANT NUMBER(s) NR 036-163 (675-021X)
9. PERFORMING ORGANIZATION NAME AND ADDRESS Naval Underwater Systems Center New London Laboratory New London, Connecticut 06320		10. PROGRAM ELEMENT, PROJECT, TASK AREA & WORK UNIT NUMBERS G1153N
11. CONTROLLING OFFICE NAME AND ADDRESS Chief of Naval Research Office of Naval Research Arlington, VA 22217		12. REPORT DATE 13 February 1985
		13. NUMBER OF PAGES 33
14. MONITORING AGENCY NAME & ADDRESS (if different from Controlling Office) Chief of Naval Research Office of Naval Research Arlington, VA 22217		15. SECURITY CLASS. (of this report) UNCLASSIFIED
		15a. DECLASSIFICATION/DOWNGRADING SCHEDULE
16. DISTRIBUTION STATEMENT (of this Report) Approved for public release; distribution unlimited.		
17. DISTRIBUTION STATEMENT (of the abstract entered in Block 20, if different from Report)		
18. SUPPLEMENTARY NOTES		
19. KEY WORDS (Continue on reverse side if necessary and identify by block number) Corrosion Pitting Nearfield Electrical Measurements Current Density Predictions Nonlinear Anodic Polarization Electric Potential Distributions Nonlinear Cathodic Polarization Electrogalvanic Fields Scanning Vibrating Electrode Technique Finite Electrical Measurements (SVET)		
20. ABSTRACT (Continue on reverse side if necessary and identify by block number) Based on completed experimental electric-field scans and the corresponding finite-element field predictions, it appears that the finite-element numerical technique presents a strong analytical tool in calculating the nearfield (within 650 μm) electric-field distributions about active microcells. This was analytically achieved with the new double membrane finite-element configuration representing nonlinear polarization and by using a local tangent slope (impedance) definition dependent on the local potential difference. The experimental determination of the normal current was realized with a newly		

20. (Cont'd)

developed scanning vibrating electrode technique (SVET). The finite-element model (FEM) developed in this report utilizes a priori measured uncoupled polarization curves for pure iron and pure copper. The current densities and the electric field intensity was calculated for all the grid points within the electrolyte and on its boundaries. Results appear to indicate that first order anodic mass loss can be predicted using finite-element predicted current density distributions on the anodic surface and the imposition of Faraday's law. The electric-field correlation established in this report for the normal current-density vector provides the confidence to proceed in the evaluation of electric fields associated with pitting and crevice corrosion.

LIBRARY
RESEARCH REPORTS DIVISION
NAVAL POSTGRADUATE SCHOOL
MONTEREY, CALIFORNIA 93943

NUSC Technical Report 7299
13 February 1985

Theoretical and Experimental Comparisons of Nearfield Electrogalvanic Fields Due to Nonlinear Polarization Layers

Rolf G. Kasper
Engineering and Technical Support Department



Naval Underwater Systems Center
Newport, Rhode Island / New London, Connecticut

Approved for public release; distribution unlimited.

Preface

This work was sponsored by the Office of Naval Research, Program Element G1153N, NR Number 036-163-(675-021X) and Research Projects RR014-11-OB and RR022-08-01. The Scientific Officer at the Office of Naval Research for this research is Dr. P. Clarkin, Code 431. This research project is entitled "Pitting and Crevice Corrosion Kinetics." The Principal Investigator is Dr. R. G. Kasper, Code 4493.

The Technical Reviewer for this report was R. S. Munn, Code 44.

Reviewed and Approved: 13 February 1985



J. F. Kelly, Jr.
Head, Engineering and Technical
Support Department

The author of this report is located at the
New London Laboratory, Naval Underwater Systems Center,
New London, Connecticut 06320.

TABLE OF CONTENTS

	Page
LIST OF ILLUSTRATIONS	ii
LIST OF TABLES	iii
INTRODUCTION	1
BACKGROUND	2
MODEL DEVELOPMENT AND BOUNDARY CONDITIONS	3
MATHEMATICAL TREATMENT OF POLARIZATION LAYERS	4
EXPERIMENTAL RESULTS	6
THEORETICAL AND EXPERIMENTAL COMPARISONS	6
SURFACE RECONFIGURATION DUE TO FARADAY'S LAW	8
CONCLUSIONS	8
REFERENCES	32
APPENDIX - DATA FROM GALVANIC CORROSION EXPERIMENTS	A-1

LIST OF ILLUSTRATIONS

Figure		Page
1	Cylindrically Symmetric Planar Galvanic Couple	19
2	Electrogalvanic Boundary Conditions	19
3	Finite-Element Model (36-deg Section)	20
4	Top View of Finite-Element Model for Iron and Copper Section . . .	20
5	Double-Membrane Representation of Polarization Layer	21
6	Axisymmetric Model of Beaker Experiment	21
7	Plane of Electrode/Electrolyte Interface	22
8	Electrolyte/Air Interface at Plane Z = 9500 μm	22
9	Defining Anodic Polarization Layer	23
10	Iron and Copper Polarization Curves	23
11	Defining Cathodic Polarization Curves	24
12	Multicell Interactions	24
13	Physical Description of Experiments	25
14	Axisymmetric Configuration and Scans for Iron/Copper Galvanic Couple	25
15	Normal Measured Current Density at Z = 650 μm , Scan 1	26
16	Normal Measured Current Density at Z = 1150 μm , Scan 2	26
17	Measured Potential of Couple at Electrolyte/Air Interface	27
18	Normal Current Density Comparisons at Z = 650 μm	27
19	Normal Current Density Comparisons at Z = 1150 μm	28
20	Current Density Versus Distance Above Electrode Surfaces at R = 0.7 mm	28
21	Potential Distribution on the Electrolyte/ Polarization Interface	29
22	Calculated Axial and Radial Current Density in the First Electrolytic Layer	29
23	Total Calculated Current Distribution in the First Electrolytic Finite-Element Layer	30
24	Anodic and Cathodic Normal Current Density Values as a Function of Radial Position	30
25	Anodic Loss Based on Faraday's Law and Finite-Element Current Density Predictions	31

LIST OF TABLES

Table		Page
1	Results of Iron (Fe) Measurements by C. R. Crowe	9
2	Results of Copper (Cu) Measurements by C. R. Crowe	10
3	Calculated Current-Density Values for Runs 6, 7, and 8, Z _{centroid} of 650 μm	11
4	Calculated Current-Density Values for Runs 6, 7, and 8, Z _{centroid} of 1125 μm	12
5	Vertical Current-Density Distribution	13
6	Potential Values at Beaker Top (FEM)	14
7	Calculated Upper- and Lower-Membrane Potentials	15
8	Average Current Density Emanating From Polarization Layer, Run 7	16
9	Calculated Values of Electric-Field Vector Above Polarization Layer, Run 7 (Z of First-Layer Centroid 27.5 μm)	18
A-1	Measured Normal Current-Density Values As a Function of Radial Distance, August 1983, Runs 15 and 18	A-2

THEORETICAL AND EXPERIMENTAL COMPARISONS OF NEARFIELD ELECTROGALVANIC FIELDS DUE TO NONLINEAR POLARIZATION LAYERS

INTRODUCTION

The characterization of localized corrosion phenomena, such as pitting and crevice corrosion, has been the focus of study for many years.¹⁻³ It is generally agreed that electrogalvanic interactions of anodic and cathodic regions inherent in real-world physical systems are very complex processes. This is particularly true because of the highly interactive coupling that exists between multiple anodes and cathodes subject to geometric effects, inhomogeneous electrolytic mediums, and polarization effects.

A number of attempts have been made to model localized corrosion using detailed models of the electrochemistry in localized regions. The idea of mathematically predicting the electrolytic corrosion behavior for a physical situation began with the work of Wagner at least four decades ago.⁴ In this pioneering work, traditional mathematical techniques were applied for predicting the potential fields of anodes and cathodes while considering the presence of geometric effects, polarization curves, and surface roughness. Analytical attempts to calculate local current distributions in the anodic/cathodic neighborhood (surfaces) generated immediate realizations that, in general, exact mathematical solutions seemed intractable except in highly specialized situations where the equations could be solved for particular geometries and simplified electrochemical situations.⁴⁻⁹ Thus, the analytical models were limited, in part, to simple geometries and constant electrolyte properties. Furthermore, the models were limited because the analyses did not take into account geometric changes of the electrode due to corrosion nor did they consider changes in composition and conductivity of the electrolyte during the course of corrosion.

In recent years, studies have been conducted that apply finite-element numerical techniques to macroscopic electrogalvanic field predictions. These models were developed for the prediction of performance of cathodically protected structures.¹⁰⁻¹⁴ Although the models did not consider changes in geometry and electrolyte properties, they were very successful in predicting current distributions at the various anodic and cathodic areas.

To effectively use the finite-element models (FEM's), sufficient electrochemical data must be measured under controlled conditions to compare model predictions with reality and to establish a data base of appropriate information. First, potential-field measurements and potential gradients at localized areas are needed to compare finite-element predictions with actual potential fields and the resultant ionic currents. The basic problem is to measure ionic currents associated with corrosion microcells. Secondly, potentiostatic polarization and impedance measurements are required as a function of electrolyte chemistry. This information is needed to update the evolution of the electrochemical-system parameters with time.

Recent advances in techniques for measuring localized currents in electrolyte solutions have made possible methods to measure ionic currents associated

with corrosion microcells. The new techniques use vibrating probes to measure currents in solution with spatial and current resolutions on the order of 15 to 20 μm and 5 nA/cm^2 , respectively. Thus, it is possible to measure corrosion currents resulting from individual local cell activity on a scale closely related to many microstructural features of materials. This is particularly useful for studies of localized corrosion phenomena, such as pitting and crevice corrosion, and in studies of composite corrosion where local galvanic effects between constituents and interfaces may be important.¹⁵

In this report, progress in the use of the finite-element method in electrogalvanic field prediction and the development of a scanning vibrating electrode technique (SVET) will be presented. The SVET has been developed for electrochemical measurements needed to test finite-element-predicted vector electrogalvanic field components. The report will cover (a) electrogalvanic FEM development, (b) mathematical treatment of polarization curves, (c) a review of the state-of-the-art of scanning vibrating probe techniques, (d) an experimental evaluation of the one-dimensional probe technique as applied to planar galvanic couples between iron and copper, and (e) a discussion of the development of a three-dimensional probe to advance the state-of-the-art.

BACKGROUND

Mathematical prediction of electrolytic corrosion behavior for a physical situation had its genesis at least four decades ago. Traditional mathematical techniques were reviewed for predicting the potential fields of anodes and cathodes in the presence of factors such as geometric effects, polarization curves, and surface roughness.⁴ Analytical attempts to calculate local current distributions in the anodic/cathodic neighborhood (surfaces) demonstrated the intractability of exact mathematical solutions.⁵

In recent years, attempts have been made to model localized corrosion through use of detailed models of the electrochemistry in localized regions. These models were limited to simple geometries and constant electrolytic properties as well as linear polarization behavior.¹⁰⁻¹⁴ The models were further limited because the analyses did not consider either geometric changes or the rate of the reaction in terms of Faraday's law.

This study investigates the use of nonlinear analysis within a subsystem of the NASA Structural Analysis (COSMIC/NASTRAN) program (Heat Transfer, Rigid Format 3) to address complex electrode boundary conditions and electrolytic interactions for a finite-element model (figure 1*). Another effort, studying the strength of a more general nonlinear finite-element program known as MARC, is also in progress.¹² Both finite-element programs are maintained on a VAX-11/780 computer at the Naval Underwater Systems Center (NUSC).

It has been clearly established in the literature⁶ that localized changes in the electrolyte chemistry occur with time and geometry during corrosion. It is, therefore, important to include these phenomena in any model dealing with localized corrosion kinetics.

*All figures have been placed together at the end of this report.

The approach to this research effort is two phased. First, numerical models are developed to describe the gradual corrosion of a surface from a planar to a pitted contour.¹⁶ The model provides corrosion information where pitting will be shown as a function of time and geometry. The model relies for its predictions on established scientific laws (conservation of charge and Faraday's) and a fixed set of physical parameters. The parameters are chosen to provide information on potential and current distributions within the electrolyte and on the anodic and cathodic surfaces. In conjunction with this effort, sufficient measurements were taken to ensure that the chosen electrochemical parameters result in predictions that will compare with reality. These measurements involved potential measurements and normal current-density measurements for two specific scans in a laboratory setup.

In general, ionic-current flow in the electrolyte is governed by the three-dimensional law of conservation of charge. In differential equation form, this law, in the absence of diffusion and convection, can be stated as

$$\nabla \cdot \vec{J} = -\frac{\partial \rho}{\partial t} . \quad (1)$$

The constitutive relationship (Ohm's law) between current density and the electric-field intensity, in terms of the electrical conductance, is

$$\vec{J} = \sigma \vec{E} , \quad (2)$$

where, by definition, the electric-field intensity is

$$\vec{E} = -\nabla \phi . \quad (3)$$

Substituting equations (3) and (2) into equation (1) yields

$$\nabla \cdot \sigma \nabla \phi = -\frac{\partial \rho}{\partial t} . \quad (4)$$

It is obvious from the above vector-field solutions that a three-dimensional spatial representation of the ionic current and the local value of the electrolyte conductivity is required to obtain a general characterization of the corrosion cell. The measurements reported in this investigation were taken for the normal component of the current density at two elevations above the polarization layer. A program was initiated to develop a directionally sensitive current-density probe (3D) to provide measurements that could be used to correlate against mathematically predicted vector-field components.

MODEL DEVELOPMENT AND BOUNDARY CONDITIONS

An FEM was developed using three-dimensional brick-type elements. Specifically, the electrolyte was represented with COSMIC/NASTRAN'S CHEXA2 and CWEDGE elements. These elements use linear interpolation functions between adjacent grid points. The general geometric feature of the electrolyte and the anodic/cathodic surfaces are shown in figure 1. The associated boundary conditions are shown in figure 2. Briefly, total current interchange between the anodic

and cathodic cell takes place between surface F'-E' and F-E. At all other surfaces, for this analysis, the gradient of the local potential function was assumed to be zero.

The overall objective of this research program is to develop a modeling and measuring capability to help us understand more fully the onset of crevice corrosion. A crevice will be defined physically as a small cavity naturally characterized in three-dimensional space. Two-dimensional and axisymmetric formulations would not be adequate for a full description. For the initial analysis, a three-dimensional model was developed using COSMIC/NASTRAN. Since the first boundary-value problem to be solved is axisymmetric, the symmetry about the z-axis was developed for 36 deg. This is shown in figures 3 and 4. At the bottom of figure 3, the entire anodic and cathodic surfaces were represented with a double layer of finite-element membrane elements. For a more detailed local representation, an upper and lower membrane structure is shown in figure 5.

In an earlier report,¹⁷ the double membrane was used successfully to incorporate nonlinear polarization curves into the nonlinear potential-field routine of COSMIC/NASTRAN. In an effort to exercise also the axisymmetric version of COSMIC/NASTRAN, a second model (figure 6) was generated using CTRAPRG elements. This model looks slightly different geometrically in that the neutral surface of the beaker is not flush with the copper surface, as shown in figure 1. In the actual experiment, at Brookhaven National Laboratory, a small lip (width of copper cell, 0.3 cm) existed at the edge of the copper ring. This model is being exercised currently using the same boundary conditions described earlier in this section.

A number of planes were identified to retrieve more easily current and voltage information from the elements and grid points, respectively. Since the measurements for the current density were performed at 650 and 1150 μm above the electrode surfaces, it was desirable to obtain current-density information at the centroid of the associated elements. The lowest plane was assumed to exist at $Z = 0$ (figure 7). The topmost plane (electrolyte/air interface) is located at $Z = 9500 \mu\text{m}$ (figure 8). The grid points identified in the middle of the figure, ranging from 3 to 554, were used to compare the calculated potential values with the measured values, to be discussed later. The details of the electric-field comparisons will be discussed fully in a later section of this report.

MATHEMATICAL TREATMENT OF POLARIZATION LAYERS

The relative impedances across the polarization layer on various electrode surfaces have a strong influence on the resulting electric fields in the electrolyte. Of course, the other boundary conditions, geometry, and conservation of current also have a significant effect on the electric and current-density fields in the medium. The approach in this study is to implement the concept of a conductive film (polarization layer) that is a function of the local

current density and the local voltage potential. Such values are given in tables 1 and 2.* These local slope values for both iron and copper are introduced into the finite-element analysis algorithm by means of table values.

For a two-cell system, the lowest measured corrosion potential and the maximum corrosion potential represent reference potentials below the sublayer (figure 5). Essentially, this states that the electric-field limits are bounded by the characteristics of the electric cell, based on measurements. However, due to geometric effects, conservation of charge, and other boundary conditions, the voltage gradients and current densities have a strong dependence on the position of the electrode because of the nonlinear relationships.

The process of defining mathematically the anodic polarization layer is illustrated in figure 9. The bottom surface in this example is defined as -0.560 volts, from measurements (figure 10) by C. R. Crowe, of the Naval Research Laboratory (NRL). Grid points 1 through 4 and a scalar point designate a space for a double-membrane finite element. The potential values at grid points 1 through 4 are unknowns in the solution process. In the center of the membrane element, a current is calculated for both the upper and lower layer. These two membranes become nonlinear control surfaces such that the average current over a small area is assumed to be a good approximation for the current-density vector emanating orthogonal to this surface. The final finite-element discretization is shown on the left with an electrolytic finite element (55 μm thick) above the polarization layer. To the right of the FEM is the measured polarization curve with the current-density vectors superposed. The current-density vector pointing up signifies anodic current whereas the vector facing down indicates cathodic current. A similar explanation can be provided for the cathodic polarization layer (figure 11). The same concept is illustrated here except that the corrosion potential for the cathode is more positive and the related current vectors face downward. The analysis will calculate all the current-density vectors at all elements and, when they are multiplied by the local elemental area, they will provide a conservation-of-current accounting system. This is illustrated schematically in figure 5 and will be discussed further in the section of this report on theoretical and experimental comparisons.

One further comment can be made regarding a multicell electrogalvanic system. If the system possessed three or more cells acting at the same time, a similar philosophy could be employed. Specifically, if cell A and cell C have the highest and lowest corrosion potential, respectively, based on polarization measurement, the scalar-point definitions for cells A and C are $\phi_{\text{CORR}}^{\text{A}}$ and $\phi_{\text{CORR}}^{\text{C}}$ (figure 12). The scalar-point definition for cell B would be $\phi_{\text{CORR}}^{\text{B}}$. The current densities for cell B may at times appear to be anodic in some regions and cathodic in other regions. By utilizing this procedure of polarization implementation, we can explore the electric-field changes in the electrolyte due to more than two cells.

*Tables have been placed together at the end of this report or in the applicable appendix.

EXPERIMENTAL RESULTS

A number of measurements were performed at Brookhaven National Laboratory by C. R. Crowe,^{17,18} of NRL, in cooperation with H. Isaacs.¹⁹ The anode and cathode were placed into an electrolytic solution, as shown in figure 13. The anode, cathode, and beaker dimensions are described in the appendix. The purpose of the experiment was to measure the current-density values at fixed elevations above anodic and cathodic surfaces. These current-density measurements are to be compared to theoretically predicted numerical models. The first scan (Run 15) and the second scan (Run 18) were performed at 650 and 1150 μm , respectively, as indicated in figure 14. The measured normal current-density values (in $\mu\text{A}/\text{cm}^2$) are given in the appendix as a function of radial distance in millimeters where $R = 0$ is the center of the circular anode and $R = 24$ mm is approximately at the outermost edge of the circular copper region. The measured values for scans 1 and 2 are plotted in figures 15 and 16, respectively.

Potential measurements also were made in the top regions of the electrolyte. The measured values were taken with respect to a standard calomel electrode. The values varied somewhat as a function of radial distance, as indicated in figure 17. The results of these measurements have been entered in a data file on a VAX-11/780 computer system to be used for comparison against calculated values from an FEM.

Several polarization curves were established for the iron and copper electrodes at pH values of 6.5 and 1.75. The data were taken by C. R. Crowe. The curves are shown in figure 10. The relevant polarization conductivity coefficients are found in tables 1 and 2 for iron and copper, respectively. These values were calculated from curve 1 and curve 2 in figure 10.

THEORETICAL AND EXPERIMENTAL COMPARISONS

The first comparison to be made will consider the results of the current-density (normal-direction) values of scan 1 (figure 15) at 650 μm above the electrode surface. The finite-element values from Run 7 (file name KASPER.NID) are given in table 3 and plotted in figure 18 against the measured values. The iron-copper interface is at a radial distance of 3.175 mm. The values from scan 2, at 1150 μm , as well as the finite-element results at 1125 μm , are plotted in figure 19. The finite-element values are given in table 4 for Run 7 and the measured values are given in table 5 for use in comparing the sensor values at various (y,z) locations with the centroidal finite-element values. The current-density results for the z-directional component look encouraging. At both elevations, it appears that the current density emanating from the anode surface is quite high with a fairly evenly distributed current-density response on the copper surface. The total current leaving the anodic surface was $+2.857612 \times 10^{-5}$ A and the total current arriving over the copper surface was -2.857670×10^{-5} A.

The current-density distribution in the vertical direction at $R = 0.7$ mm (centroid of CWEDGE element nearest to the origin) was calculated from the same finite-element run. The calculated numbers and some limited measured data

are given in table 5. In figure 20, the calculated vertical current-density amplitude correlates fairly well with the measured values. It should be noted that both current vectors, J_Z and J_R , approach zero at the top of the electrolyte ($Z = 9.5$ mm).

The remaining measurements for comparison with the FEM were of the potential distribution at the top of the electrolyte. A distribution of the measured potentials is illustrated in figure 17 by Crowe. Those values, along with the finite-element results, are given in table 6. The measured and the predicted finite-element values are plotted in figure 21. It appears that the calculated values vary less than 5 percent as a function of position. Both distributions, however, do show a dip in the potential distribution near $R = 0$ (center).

In the area of the polarization layer, the local polarization effects could be observed on an element-to-element basis. The grid points on the edge of the electrolyte (upper layer on the membrane) on both the iron and copper area appear to show a gradual (table 7) potential distribution for the model. This distribution is shown as the series of circular data points in figure 21. The anodic and cathodic polarization also is shown quite dramatically in figure 21 by the crossed data points. The anodic effects can be seen between $R = 0$ and $R = 0.3175$ cm, with a fairly noticeable change in the anodic distribution for the four grid points. The potential distribution in the cathodic area appears more uniform except near the iron/copper interface. Related to this potential gradient is the current density emanating from this polarization layer. In this case, the average current density was recorded (table 8) from the FEM. Clearly, it appears that the current density from the center of the iron polarization layer is maximum and that the current density going into the copper surface is considerably lower and also more uniform.

In the first electrolytic layer (element centroid at $Z = 27.5$ μm), the average axial- and radial-current density were calculated and recorded in table 9. As a function of radial position, the radial-current and axial-current density was plotted in figure 22. The axial component and the radial vector component appear to be maximum in the center of the anodic-electrode surface. The rate of decay is greater for the axial component than for the radial component for the first 5 to 7 mm. The axial current-density and the radial current-density vectors are denoted with circular and crossed data points, respectively. The radial current-density vector is always positive, whereas the axial component is only positive on and near the anodic-electrode surface. Therefore, in the first electrolyte layer, the total current-density vector can be represented approximately by the distribution indicated in figure 23. In a global sense, this figure clearly shows that the vector field reverses slightly beyond the iron/copper interface at $Z = 27.5$ μm . The total current leaving the anode and that arriving at the cathode are $+2.857612 \times 10^{-5}$ A and -2.857670×10^{-5} A, respectively.

The numerical results, when related to the measured polarization curves, seem to show the following. In the center of the anodic electrode, the model predicts an average current density of 37.8 A/m². This current-density state is indicated on the measured polarization curve as number 1 in figure 24. The second element on the anodic-electrode surface appears to have an average current density of 6.3 A/m² (table 8) and is denoted as element 2 in figure 24. The third element on the anodic-electrode surface was calculated to be

4.13 A/m². That point, also, is shown in figure 24 as the last anodic theoretical point. The first cathodic element (number 4) was calculated to be -8.52×10^{-2} A/m² (table 8). Most of the remaining cathodic-electrode states, elements 5 through 12, were calculated to be, on the average, approximately -1.35 to -1.4×10^{-1} A/m².

SURFACE RECONFIGURATION DUE TO FARADAY'S LAW

Based on the encouraging correlation between the finite-element predictions and the measured results in the nearfield of the electrode surfaces, it would appear reasonable to impose Faraday's law to determine the amount of iron mass leaving the anode as a function of time and position. Faraday's law states⁵ that the mass rate can be expressed as

$$\text{Rate (gr/sec} \cdot \text{cm}^2) = \frac{JA}{nF}, \quad (5)$$

where A is the atomic weight, n is the valence number, J is the current density, and F is defined as 96,500 coulombs/mole electron. For pure iron, A = 55.8 and n = 2. The calculated current density for the first finite element on the electrode surface was 37.8048 A/m². According to table 8, the second and third finite-element results indicate a normal current density of 6.2835 and 4.13834 A/m², respectively. Substituting values into equation (5) for the first element, we have a material loss rate of 0.0109×10^{-4} g/s \cdot cm². This rate translates into a loss of approximately 0.6 grams per week \cdot cm² for the first element. The second anodic-surface element would experience a loss of approximately 16 percent of the first element. The third element would experience a rate loss of approximately 11 percent of that predicted for the first element. Since the mass rate is proportional to the current density in the local regions of a given galvanic cell, an approximate reconfiguration of the anodic-electrode surface can be attempted for time greater than zero. In figure 25a, the anodic surface is illustrated at time equal to zero. Assuming that the nonlinear polarization curves at t = 0 and the ph factor of 1.75 at t = 0 remain constant for the next increment of time, it might be speculated that the new electrode surfaces may take on the geometry illustrated in figure 25b at time equal to one month.

At a certain point in time, the initial polarization curves need to be updated because of the changes in the electrolyte and the geometric surface changes on the electrode. This type of experiment and analysis will be attempted in the next year. It will involve the addition of a newly developed three-dimensional electric-field probe and perhaps higher-ordered finite elements.

CONCLUSIONS

Based on the completed experimental electric-field scans and the corresponding finite-element field prediction, it appears that the finite-element technique presents a strong analytical tool in calculating the nearfield electric-field distributions about active electrode surfaces. The FEM described

in this report made reference to an a priori measured set of uncoupled polarization curves for pure iron and pure copper. Based on a local tangent slope definition dependent totally on the local potential difference at a given position in space or on the electrode surface, the current densities were calculated everywhere.

The electric-field correlation established in this report for the normal current-density vector provides the confidence to proceed in the evaluation of electric fields associated with pitting and crevice corrosion. Experiments and model developments presently are being planned for the next fiscal year. They will involve more multicellular activities, inhomogeneous conductivity distribution in the electrolyte, and the role of time variation.

Table 1. Results of Iron (Fe) Measurements by C. R. Crowe*

ϕ_1	ϕ_2	i_1 (A/m ²)	i_2 (A/m ²)	$h = \left \frac{i_2 - i_1}{\phi_2 - \phi_1} \right $
+10.0	0.0			
-0.410	-0.460	10×10^1	5×10^1	1000
-0.460	-0.500	5×10^1	2×10^1	750
-0.500	-0.54	2×10^1	6×10^0	350
-0.54	-0.56	6×10^0	1.4×10^0	230
-0.56	-0.58	1.4×10^0	3.2×10^0	45
-0.58	-0.595	3.2×10^0	5×10^0	120
-0.595	-0.605	5×10^0	8×10^0	300
-0.605	-0.670	8×10^0	20	184.6
-0.670	-0.76	2×10^1	5×10^1	333.33
-0.76	-0.82	5×10^1	7.5×10^1	416
-0.82	-0.92	7.5×10^1	10×10^1	250
-10.0	0.0			

*Performed on 24 January 1984.

Table 2. Results of Copper (Cu) Measurements by C. R. Crowe*

ϕ_1	ϕ_2	i_1 (A/m ²)	i_2 (A/m ²)	$h = \left \frac{i_2 - i_1}{\phi_2 - \phi_1} \right $
+10.0	0.0			
-1.2×10^{-1}	-1.4×10^{-1}	10^1	4×10^0	
-0.12	-0.14	10	4.0	300
-0.14	-0.18	4	1.0	75.00
-0.18	-0.20	1	0.4	30
-0.20	-0.24	0.4	0.12	7.0
-0.24	-0.27	0.12	0.03	3.0
-0.27	-0.28	0.03	0.01	2.0
-0.28	-0.285	0.01	0.03	4.0
-0.285	-0.320	0.03	0.06	0.857
-0.320	-0.355	0.06	0.10	1.143
-0.355	-0.38	0.10	0.20	0.25
-0.38	-0.418	0.20	0.40	5.26
-0.418	-0.440	0.40	0.7	13.636
-0.440	-0.485	0.7	2.0	28.888
-0.485	-0.520	2.0	4.0	57.14
-0.520	-0.580	4.0	10.0	100.0
-10.0	0.0			

*Performed on 27 January 1984.

Table 3. Calculated Current-Density Values for Runs 6, 7, and 8,
 Z_{centroid} of 650 μm^*

Element		R (m)	J _Z (μA/cm ²)		
			Run 6, Z = 500 μm	Run 7, Z = 650 μm	Run 8, Z = 600 μm
149	WEDGE	0.0007	+1619.28	+1599.27	1606.789
154	HEXA2	0.001786	+900.50	821.075	850.23
164	HEXA2	0.002778	264.024	+246.00	252.056
217	WEDGE	0.004375	+53.55	+61.34	58.1359
183	HEXA2	0.005897	3.490	5.68389	4.673
194	HEXA2	0.007713	-8.783	-7.133	-7.7438
204	HEXA2	0.00973	-11.67	-10.757	-11.1198
214	HEXA2	0.01129	-11.701	-10.948	-11.272
229	HEXA2	0.013875	-12.159	-11.634	-11.863
239	HEXA2	0.017125	-13.44	-13.16	-13.25
249	HEXA2	0.020375	-13.53	-13.084	-13.31
259	HEXA2	0.023625	-9.241	-8.85	-9.0408

*Width of the first solid electrolytic element for Run 6 is 250 μm , for Run 7 it is 550 μm , and for Run 8 it is 450 μm .

Table 4. Calculated Current-Density Values for Runs 6, 7, and 8,
 Z_{centroid} of 1125 μm^*

Element		R (m)	J_Z ($\mu\text{A}/\text{cm}^2$)		
			Run 6, $Z = 25 \mu\text{m}$	Run 7, $Z = 55 \mu\text{m}$	Run 8, $Z = 45 \mu\text{m}$
294	WEDGE	0.0007	1013.70	1010.256	1008.75
300	HEXA2	0.001786	639.98	640.64	641.23
309	HEXA2	0.0027785	271.35	272.22	272.87
362	WEDGE	0.004375	81.424	81.386	81.176
329	HEXA2	0.0058975	+20.017	19.998	19.998
339	HEXA2	0.007713	-1.8024	-1.831	-1.821
349	HEXA2	0.00973	-8.172	-8.1539	-8.1634
359	HEXA2	0.001129	-10.967	-10.881	-10.91
374	HEXA2	0.013875	-12.073	-12.016	-12.035
384	HEXA2	0.017125	-12.24	-12.264	-12.207
394	HEXA2	0.020375	-12.025	-12.016	-12.016
404	HEXA2	0.023625	-8.268	-8.258	-8.3065

*Width of the first solid electrolytic element for Run 6 is 250 μm ,
 for Run 7 it is 550 μm , and for Run 8 it is 450 μm .

Table 5. Vertical Current-Density Distribution

Z (cm)	Finite-Element Results		Crowe Measured Data*
	J_Z (A/m ²)	J_R (A/m ²)	
0.275	18.515	7.7166	
0.650	15.99	5.25	10.93
1.125	10.10	3.15	
1.150			9.19
2.25	4.552	1.60	
3.75	2.3799	0.75	
5.75	0.9164	0.37	
8.25	0.250	0.245	

*Linearly adjusted from $R = 0$ and $Z = 1150 \mu\text{m}$ to $R = 0.7 \text{ mm}$, $Z = 650 \mu\text{m}$, and $R = 0.7 \text{ mm}$, $Z = 1150 \mu\text{m}$.

Table 6. Potential Values at Beaker Top (FEM)

Grid Point	Z (m)	R (m)	H (First Layer)			Potential Measurements
			Run 6, 250 μ m	Run 7, 550 μ m	Run 8, 450 μ m	
554	0.0095	0.0	-0.4773032	0.4773342	0.477309	-0.478
531		0.001191	-0.4772575	0.4772889	0.477264	
507		0.002381	-0.4772152	-0.4772465	-0.4772215	
683		0.003175	-0.4771854	-0.4772167	-0.477191	-0.465
444		0.004990	-0.4770645	-0.4770958	-0.477070	
364		0.008622	-0.4768495	-0.4768808	-0.476855	
324		0.01044	-0.4767558	-0.4767871	-0.476762	
284		0.01225	-0.4766748	-0.4767061	-0.47668	-0.465
244		0.01550	-0.4765598	-0.4765910	-0.476566	
204		0.01875	-0.4764823	-0.4765135	-0.4764886	
164		0.0220	-0.4764353	-0.4764665	-0.4764416	
124		0.02525	-0.4764101	-0.4764413	-0.4764160	-0.460
83		0.03150	-0.4763968	-0.4764280	-0.4764030	
43		0.03775	-0.4763949	-0.4764261	-0.4764011	
3	0.00950	0.0440	-0.4763947	-0.4764259	-0.4764009	-0.459

Table 7. Calculated Upper- and Lower-Membrane Potentials

UPPER.DAT;1		LOWER.DAT;1	
0.000000E+00	-0.4841611	0.000000E+00	-0.5409910
1.191000	-0.4821011	1.191000	-0.5025470
2.382000	-0.4794905	2.382000	-0.4785590
3.175000	-0.4785227	3.175000	-0.4838132
4.990000	-0.4776031	4.990000	-0.3145340
6.805000	-0.4771680	6.805000	-0.3074600
8.620000	-0.4769190	8.620000	-0.3133700
10.44000	-0.4767500	10.44000	-0.3152500
12.25000	-0.4766390	12.25000	-0.3129100
15.50000	-0.4764952	15.50000	-0.3086500
18.75000	-0.4764148	18.75000	-0.3071943
22.00000	-0.4763770	22.00000	-0.3075860
25.25000	-0.4763978	25.25000	-0.3073680

Table 8. Average Current Density Emanating From Polarization Layer, Run 7

Element	Total Area ($\times 10^{-6} \text{ m}^2$)	I, Upper Layer (A)	I, Lower Layer (A)	Averages		Run 7 Radial (Centroids) (m)
				I (A)	J (A/m ²)	
1, 2	0.2228145 One element	+7.063891 $\times 10^{-6}$	+9.783044 $\times 10^{-6}$	8.42348 $\times 10^{-6}$	37.8048	0.0007
3, 4	0.668443 One element	+6.34566 $\times 10^{-6}$	2.054681 $\times 10^{-6}$	4.200171	6.2835133	0.001786
5, 6	0.469388 One element	1.470196 $\times 10^{-6}$	2.414781 $\times 10^{-6}$	1.942488	4.1383429	0.00227785
7, 8, 9	2.327838 Three elements	Total -17.26038 $\times 10^{-8}$	Total -22.428868 $\times 10^{-8}$	-19.844624 $\times 10^{-8}$	-8.5249163 $\times 10^{-2}$	0.004375
14, 15	3.3627494 Two elements	-4.802786 $\times 10^{-7}$	-5.30171 $\times 10^{-7}$	-5.052248 $\times 10^{-7}$	-1.502416 $\times 10^{-1}$	0.0058975
18, 19	4.403078 Two elements	-6.425913 $\times 10^{-7}$	-5.965633 $\times 10^{-7}$	-6.195773 $\times 10^{-7}$	-1.4071459 $\times 10^{-1}$	0.007713

Table 8. (Cont'd) Average Current Density Emanating From Polarization Layer, Run 7

Element	Total Area ($\times 10^{-6} \text{ m}^2$)	I, Upper Layer (A)	I, Lower Layer (A)	Averages		Run 7 Radial (Centroids) (m)
				I (A)	J (A/m ²)	
42, 43	5.443551 Two elements	-8.044797 $\times 10^{-7}$	-6.764014 $\times 10^{-7}$	-7.404405 $\times 10^{-7}$	-1.3602161 $\times 10^{-1}$	0.00973
22, 23	6.451088 Two elements	-9.524385 $\times 10^{-7}$	-8.011006 $\times 10^{-7}$	-8.767696 $\times 10^{-7}$	-1.3591034 $\times 10^{-1}$	0.01129
26, 27	14.1666621 Two elements	-2.105983 $\times 10^{-6}$	-1.952647 $\times 10^{-6}$	-2.029315 $\times 10^{-6}$	-1.4324623 $\times 10^{-1}$	0.013875
30, 31	17.484928 Two elements	-2.515855 $\times 10^{-6}$	-2.578321 $\times 10^{-6}$	-2.547088 $\times 10^{-6}$	-1.4567335 $\times 10^{-1}$	0.017125
34, 35	20.803237 Two elements	-3.002071 $\times 10^{-6}$	-2.980099 $\times 10^{-6}$	-2.9959855 $\times 10^{-6}$	-1.44015 $\times 10^{-1}$	0.020375
38, 39	24.12154 Two elements	-3.480185 $\times 10^{-6}$	-3.485510 $\times 10^{-6}$	-3.4828475 $\times 10^{-6}$	-1.4438744 $\times 10^{-1}$	0.023625

Table 9. Calculated Values of Electric-Field Vector Above Polarization Layer, Run 7 (Z of First Layer Centroid 27.5 μm)

Element	R (m)	J _{Zave} (A/m ²)	J _{Rave} (A/m ²)
4, 5 (WEDGE)	0.0007	+18.515	7.7166
154, 155 (HEXA2)	0.001786	+8.2107	7.2043
164, 165 (HEXA2)	0.0027785	+2.460	5.1157
217, 218 (WEDGE)	0.004375	+0.6130	2.663
183, 184 (HEXA2)	0.0058975	+0.05683	1.3665
194	0.007713	-0.071334	+0.83534
204	0.00973	-1.0757	+0.55484
214	0.01129	-1.0948	+0.39613
229	0.013875	-0.11634	0.25575
239	0.017125	-0.131607	0.150716
249	0.020375	-0.130844	0.070059
259	0.023625	-0.08850	-0.0020349

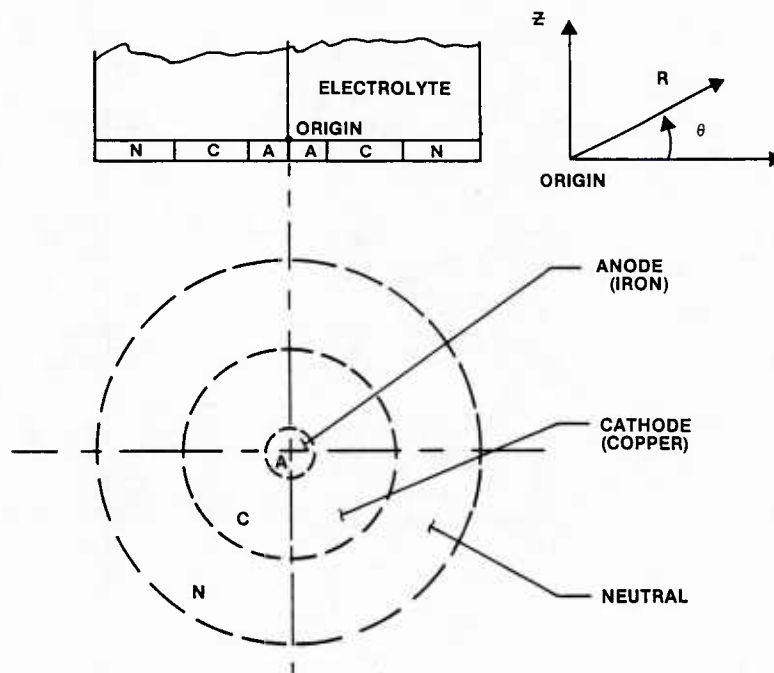


Figure 1. Cylindrically Symmetric Planar Galvanic Couple

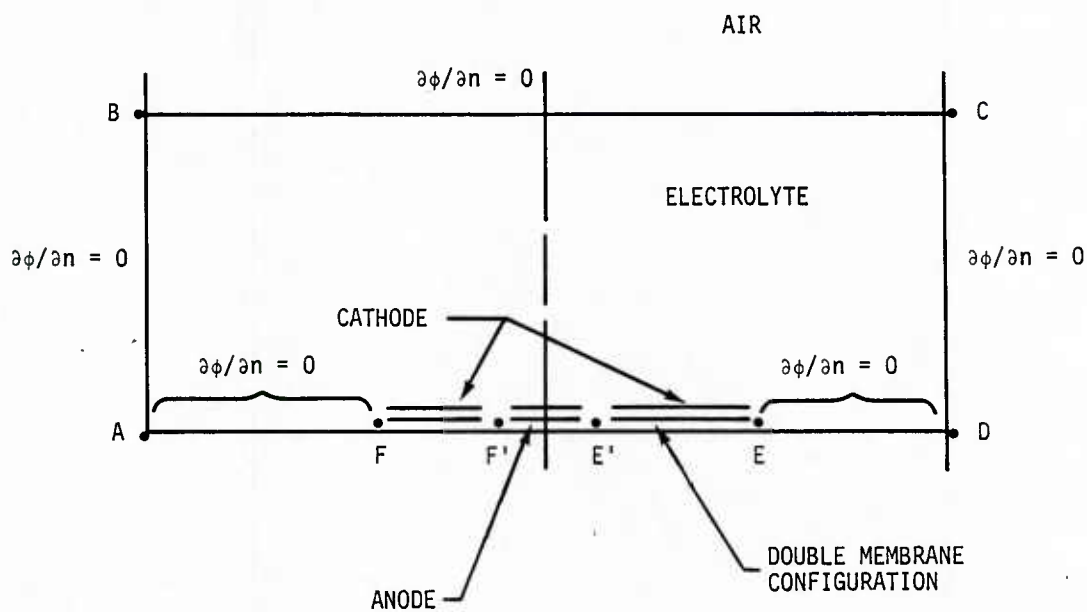


Figure 2. Electrogalvanic Boundary Conditions

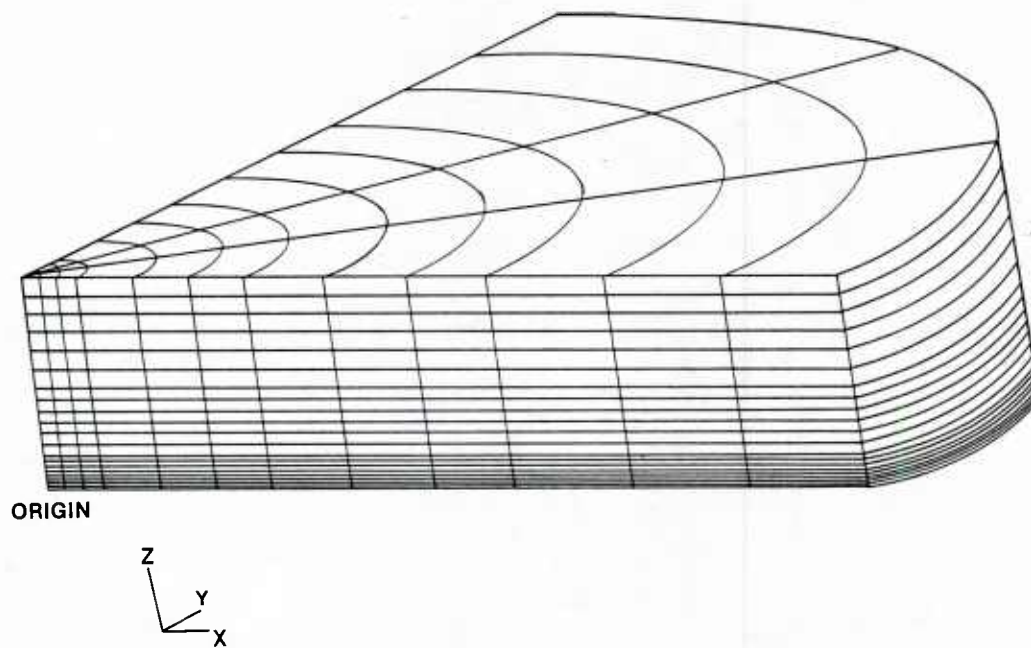


Figure 3. Finite-Element Model (36-deg Section)

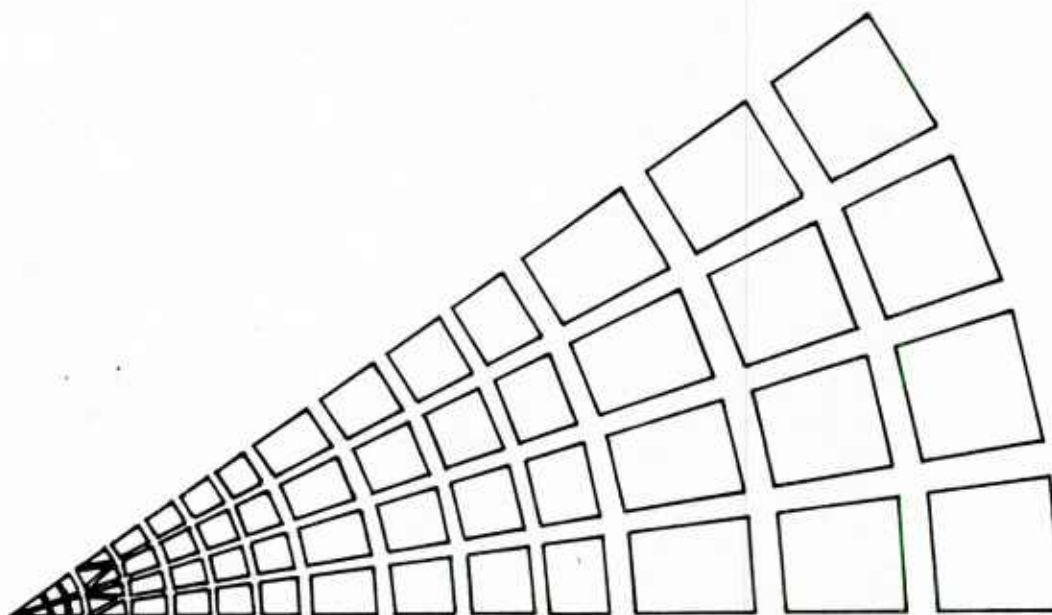


Figure 4. Top View of Finite-Element Model
for Iron and Copper Section

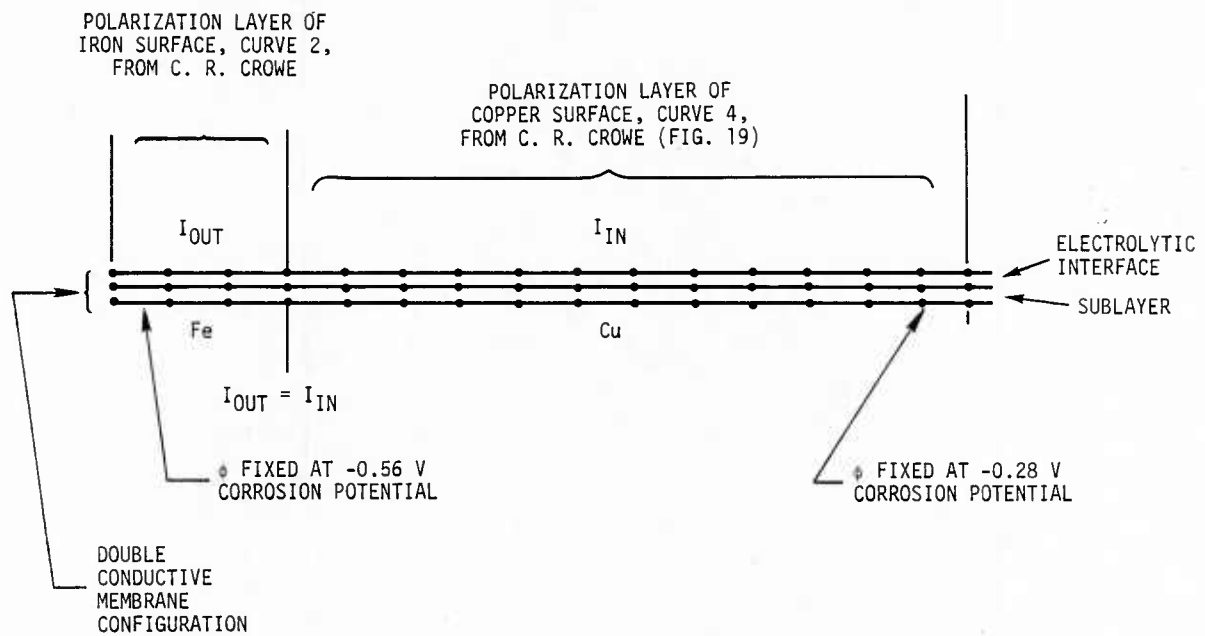


Figure 5. Double-Membrane Representation of Polarization Layer

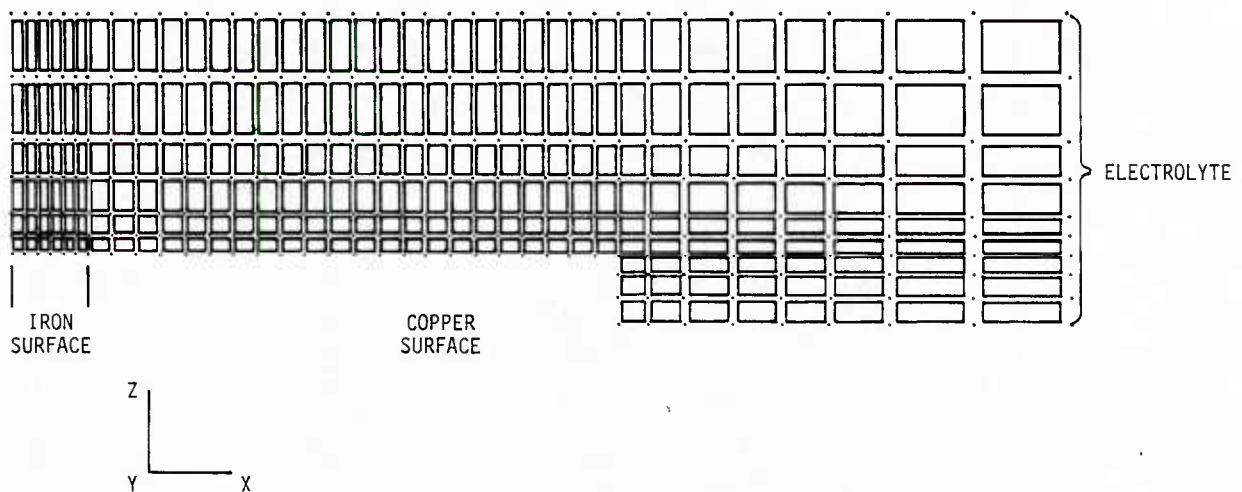


Figure 6. Axisymmetric Model of Beaker Experiment

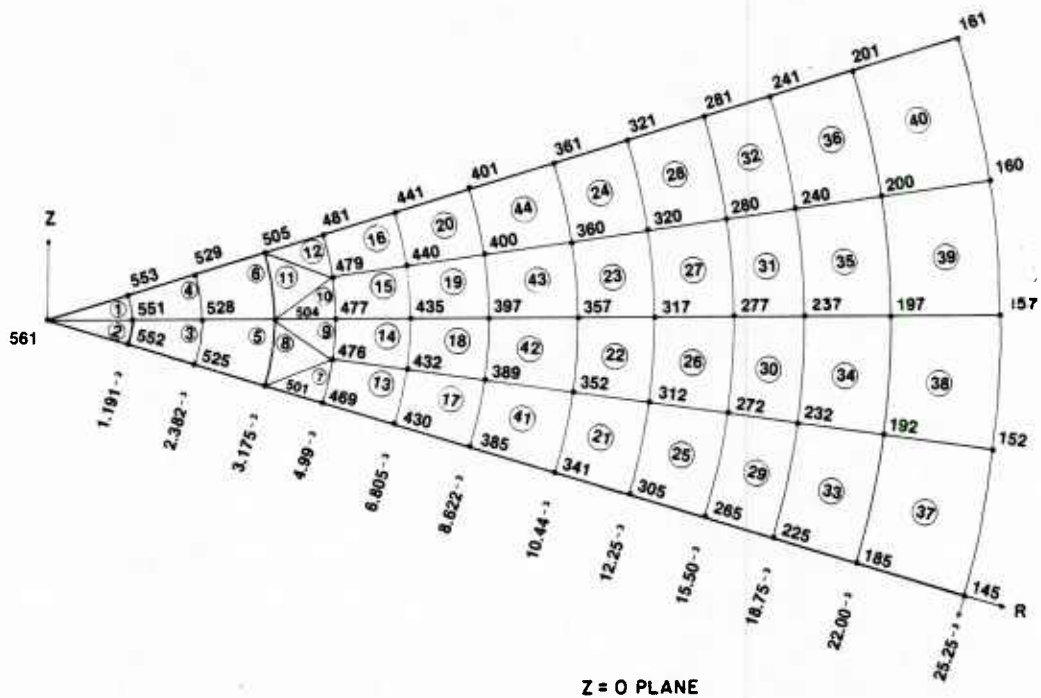


Figure 7. Plane of Electrode/Electrolyte Interface

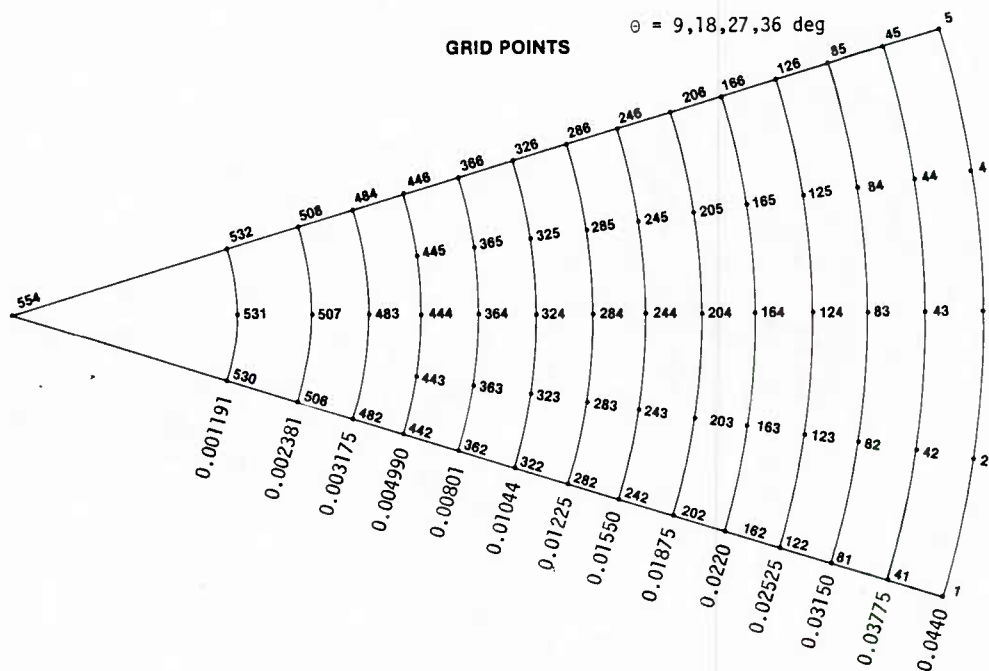


Figure 8. Electrolyte/Air Interface at Plane $Z = 9500 \mu\text{m}$

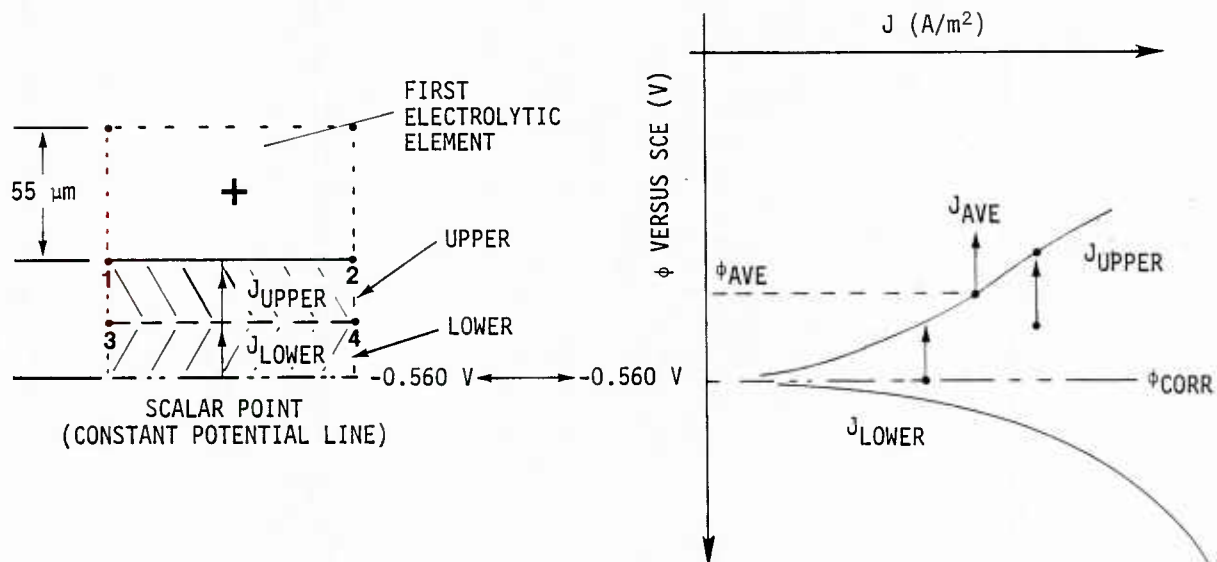


Figure 9a. Finite-Element Representation

Figure 9b. Polarization Data

Figure 9. Defining Anodic Polarization Layer

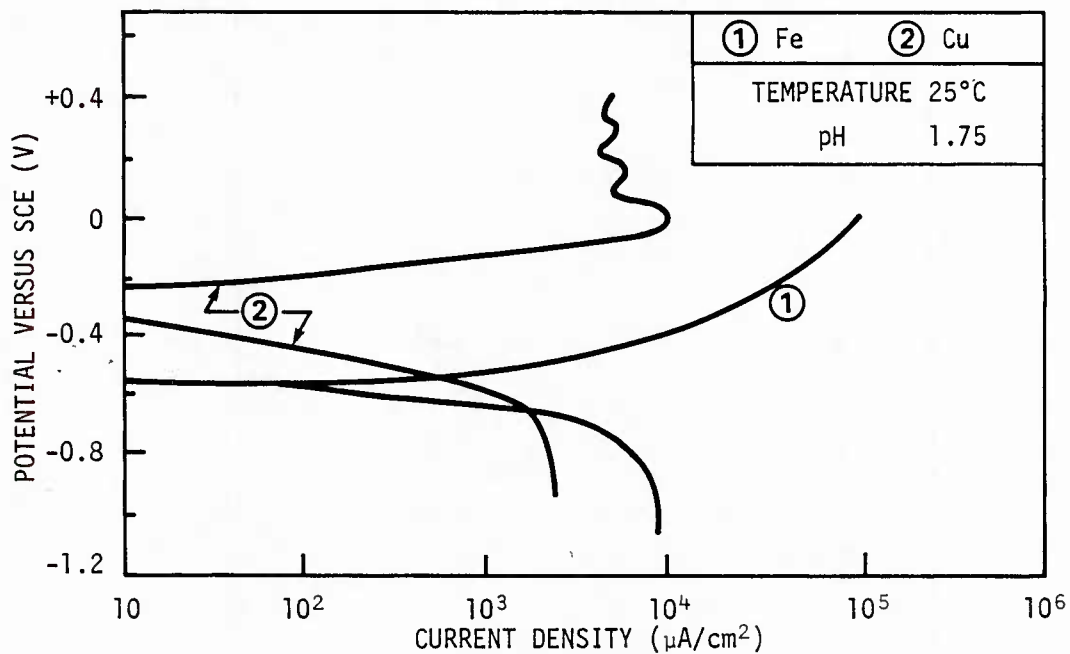


Figure 10. Iron and Copper Polarization Curves

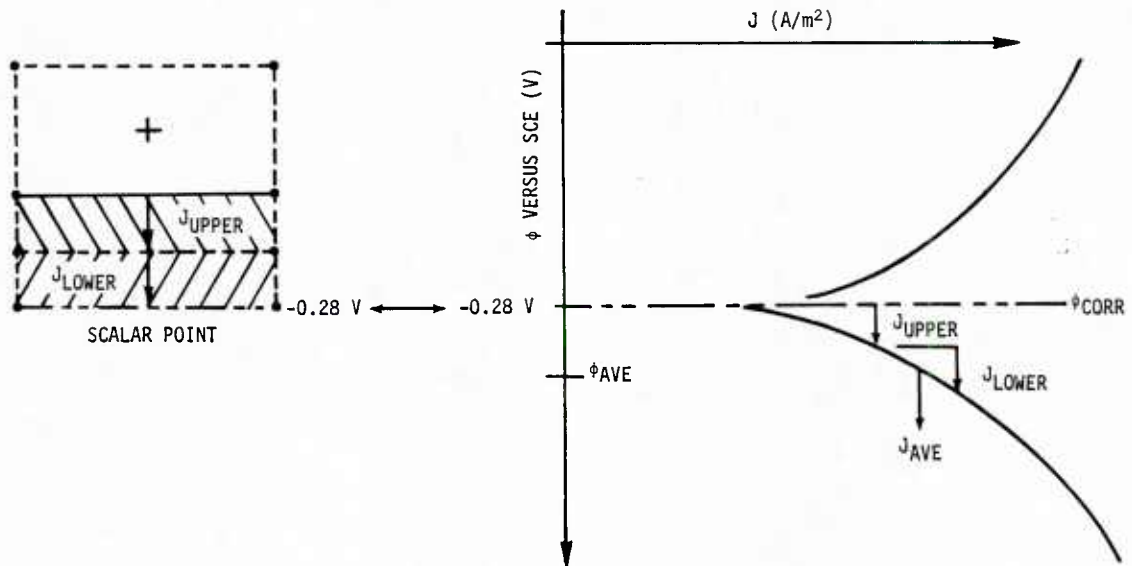


Figure 11a. Finite-Element Representation

Figure 11b. Polarization Data

Figure 11. Defining Cathodic Polarization Curves

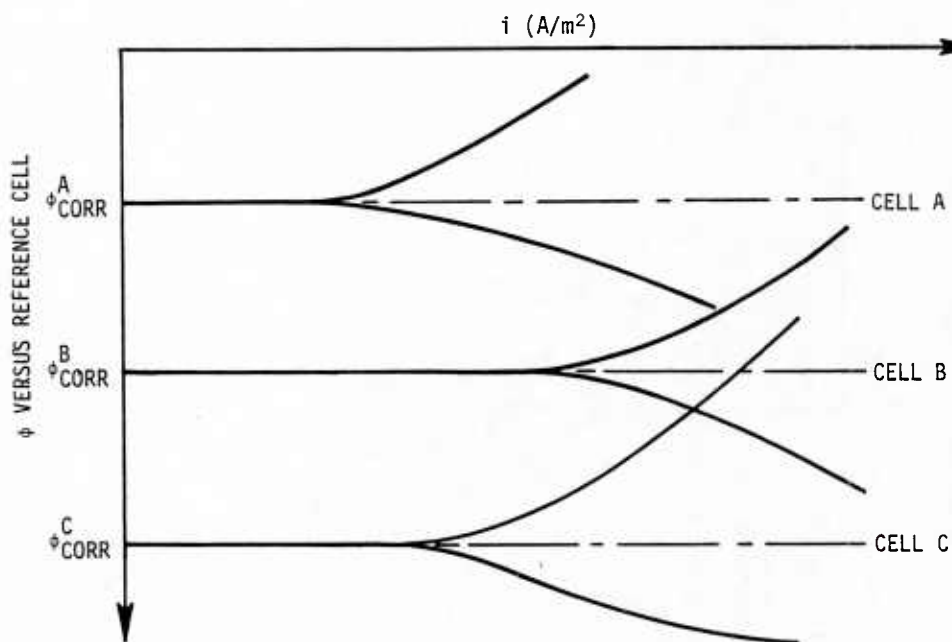


Figure 12. Multicell Interactions

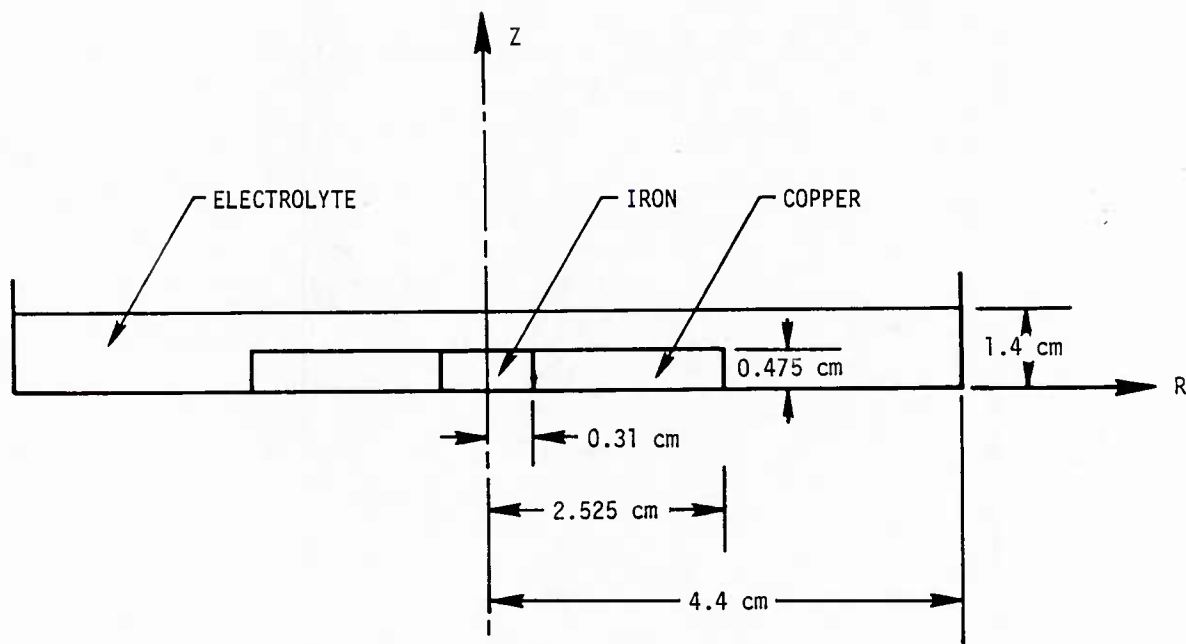


Figure 13. Physical Description of Experiments

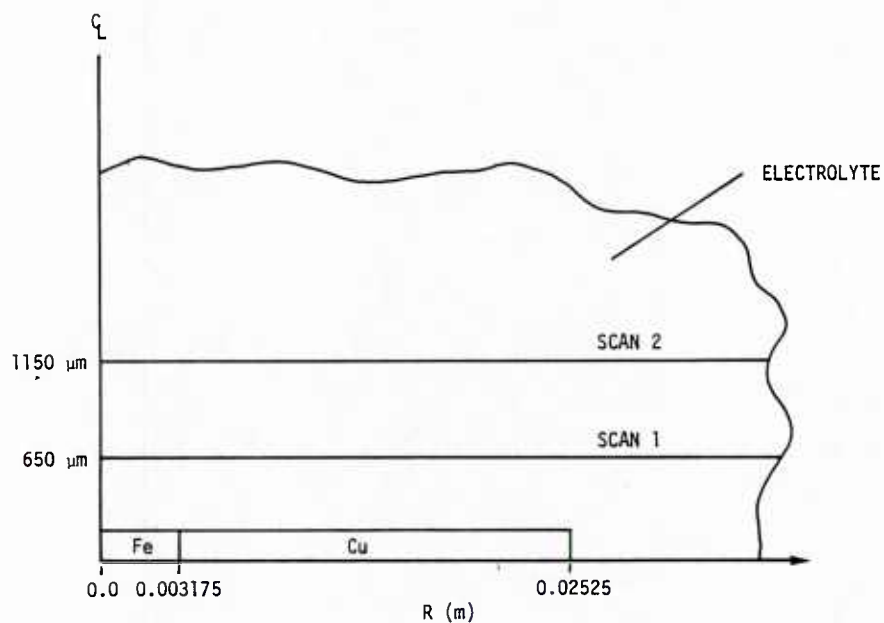


Figure 14. Axisymmetric Configuration and Scans for Iron/Copper Galvanic Couple

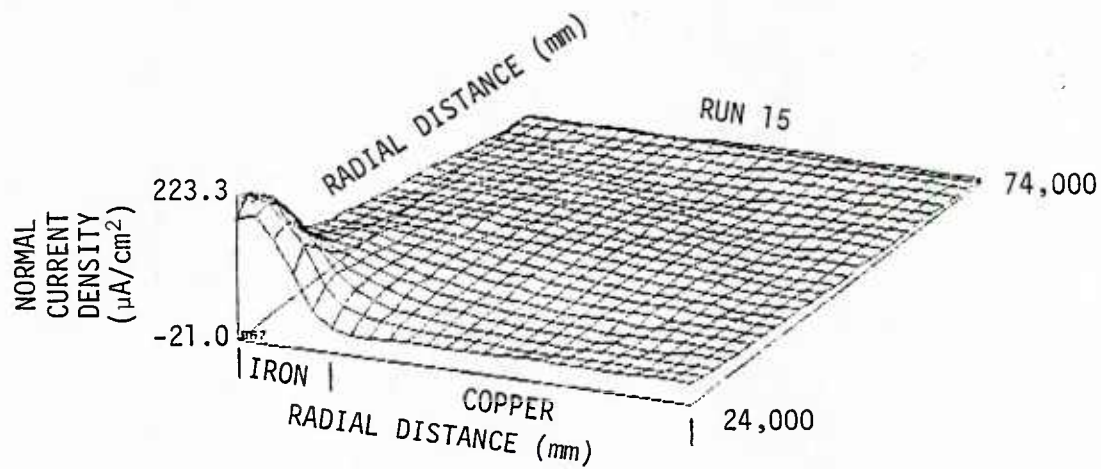


Figure 15. Normal Measured Current Density
at $Z = 650 \mu\text{m}$, Scan 1

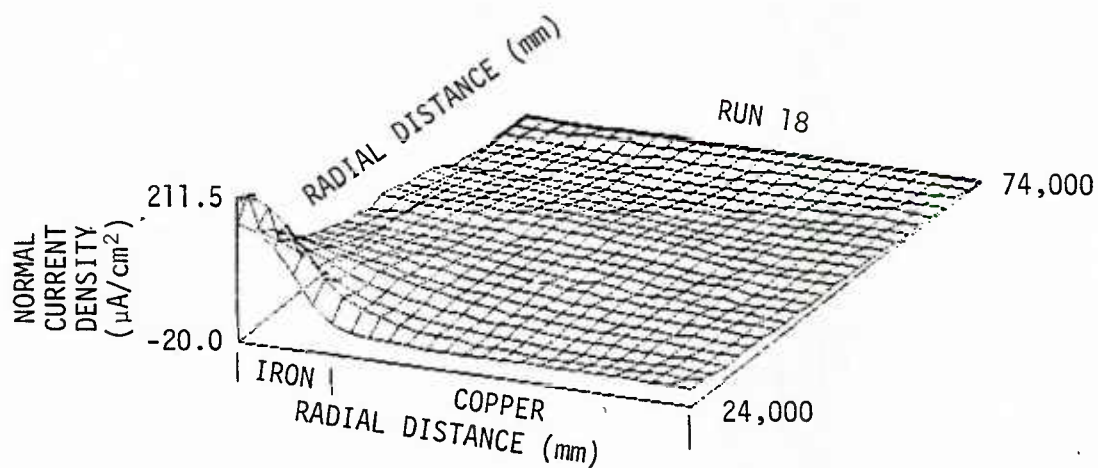


Figure 16. Normal Measured Current Density
at $Z = 1150 \mu\text{m}$, Scan 2

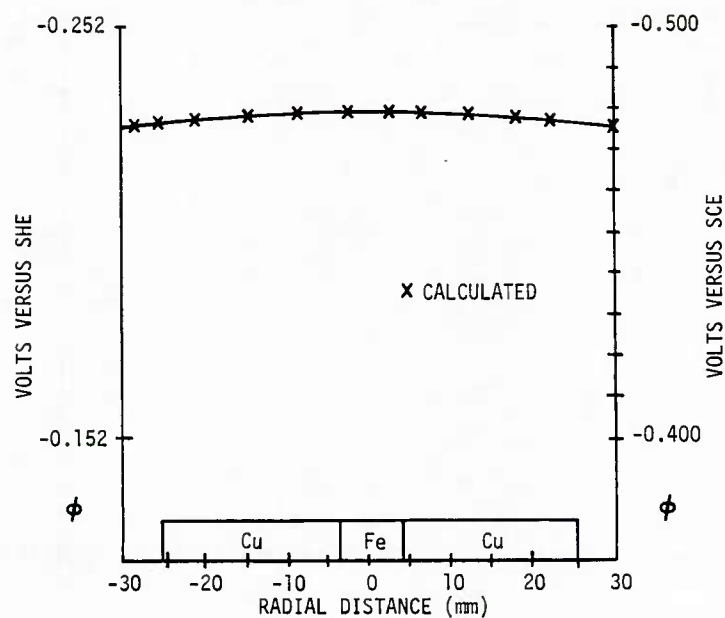


Figure 17. Measured Potential of Couple at Electrolyte/Air Interface

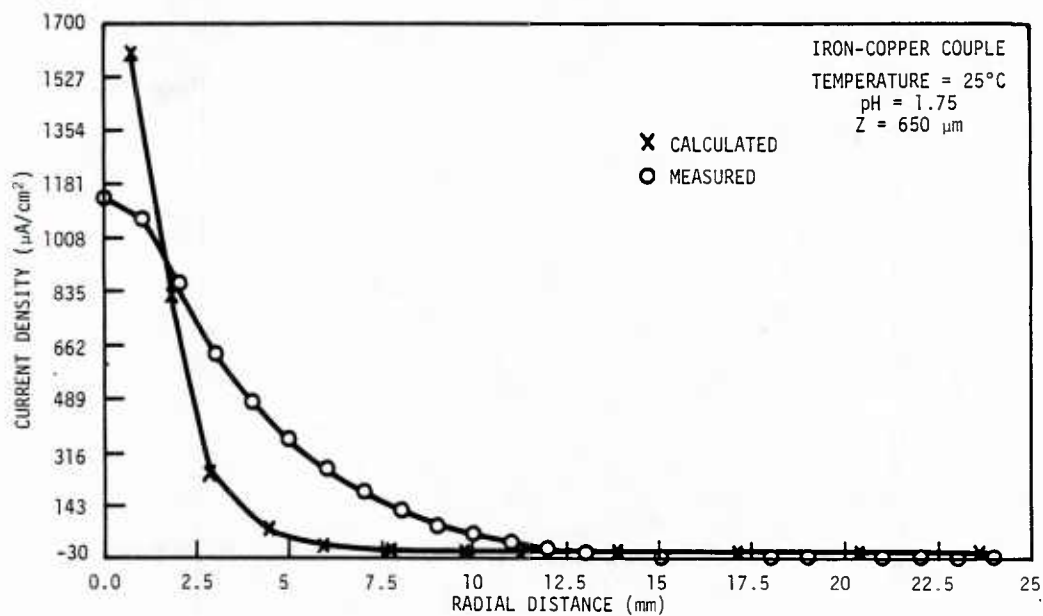


Figure 18. Normal Current Density Comparisons at Z = 650 μm

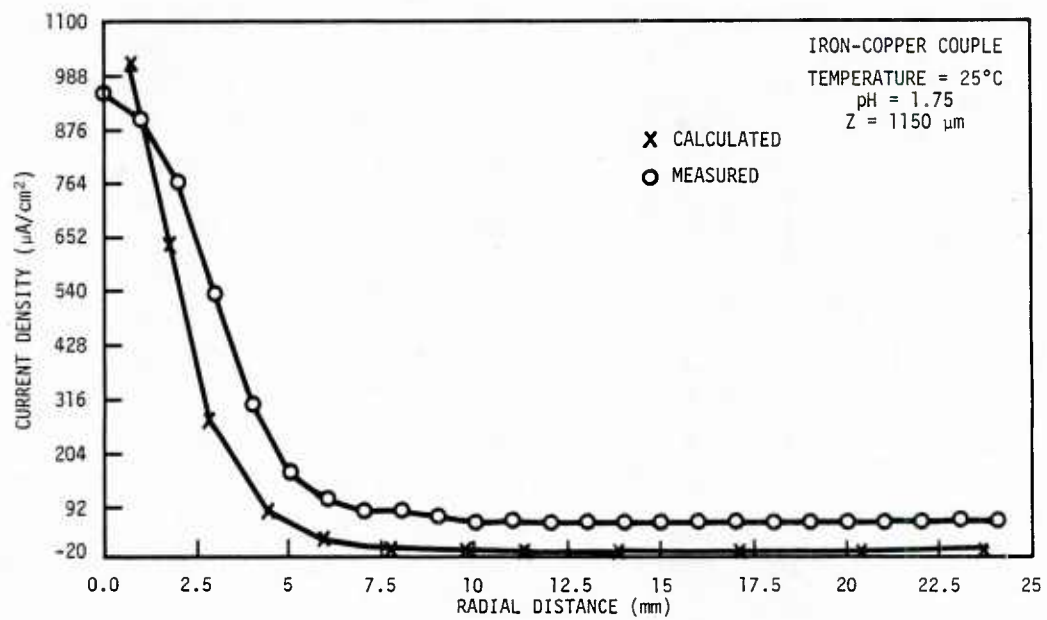


Figure 19. Normal Current Density Comparisons
at Z = 1150 μm

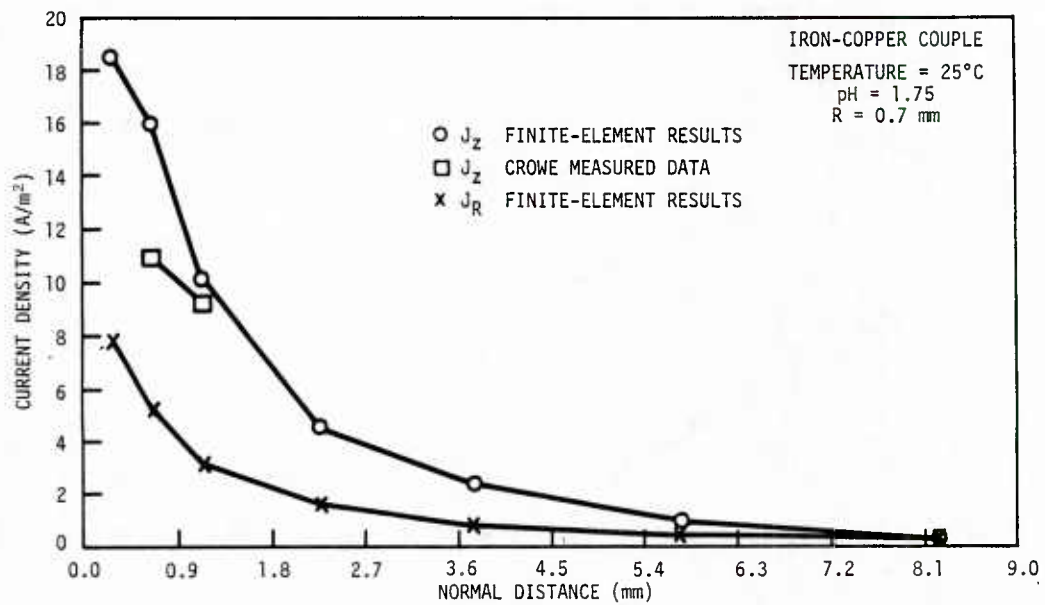


Figure 20. Current Density Versus Distance Above
Electrode Surfaces at R = 0.7 mm

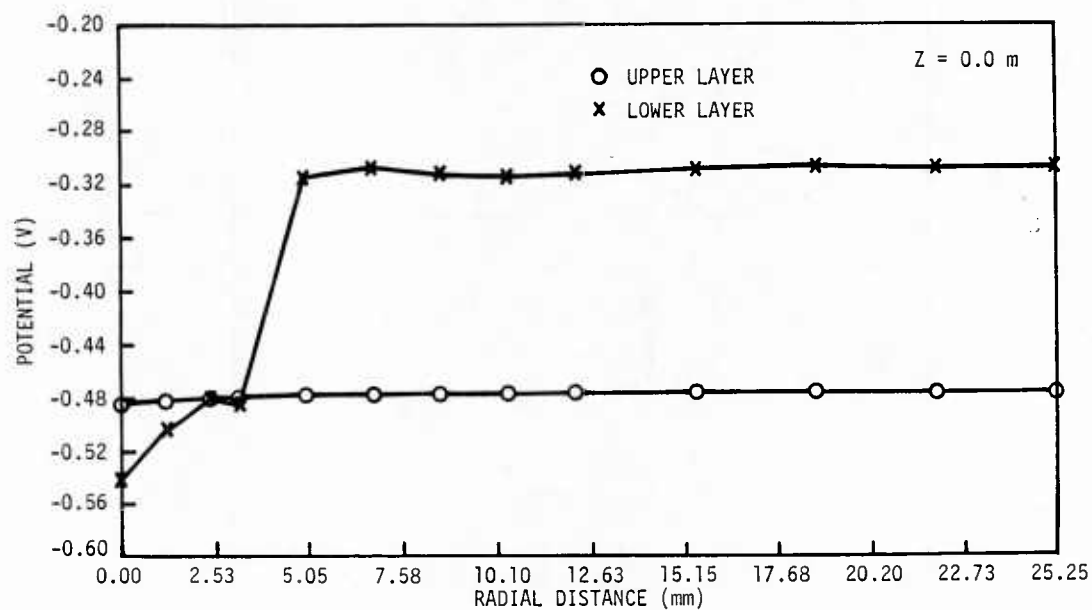


Figure 21. Potential Distribution on the Electrolyte/Polarization Interface

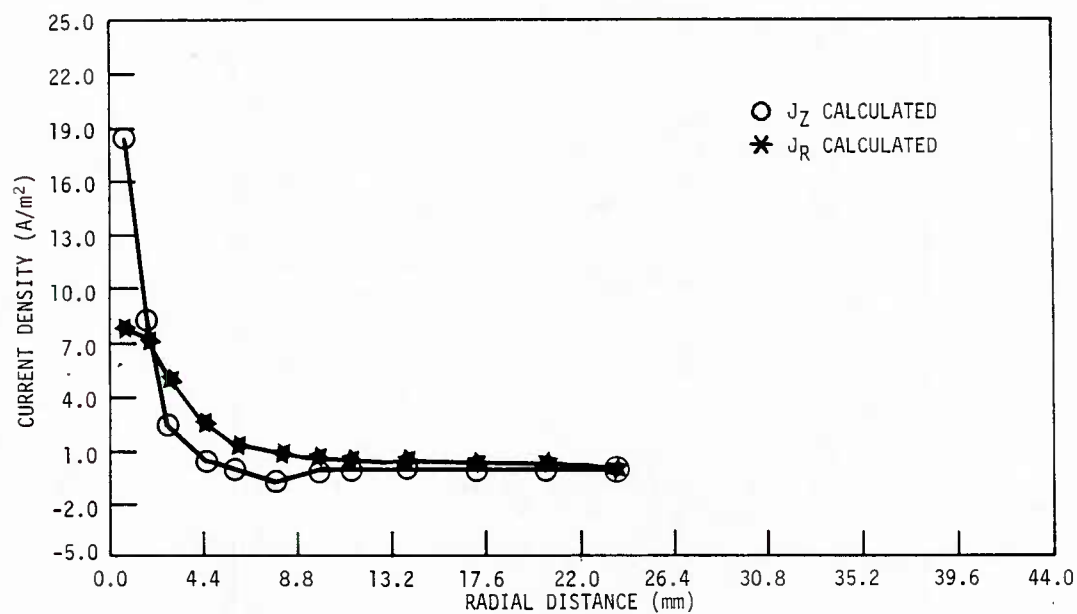


Figure 22. Calculated Axial and Radial Current Density in the First Electrolytic Layer

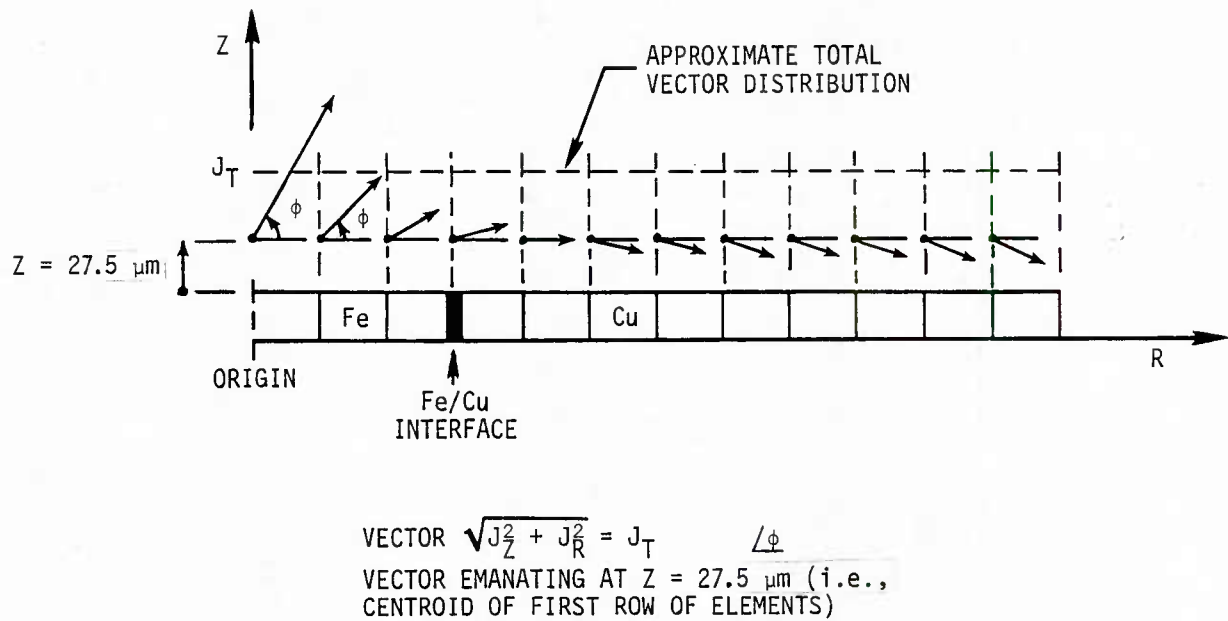


Figure 23. Total Calculated Current Distribution in the First Electrolytic Finite-Element Layer

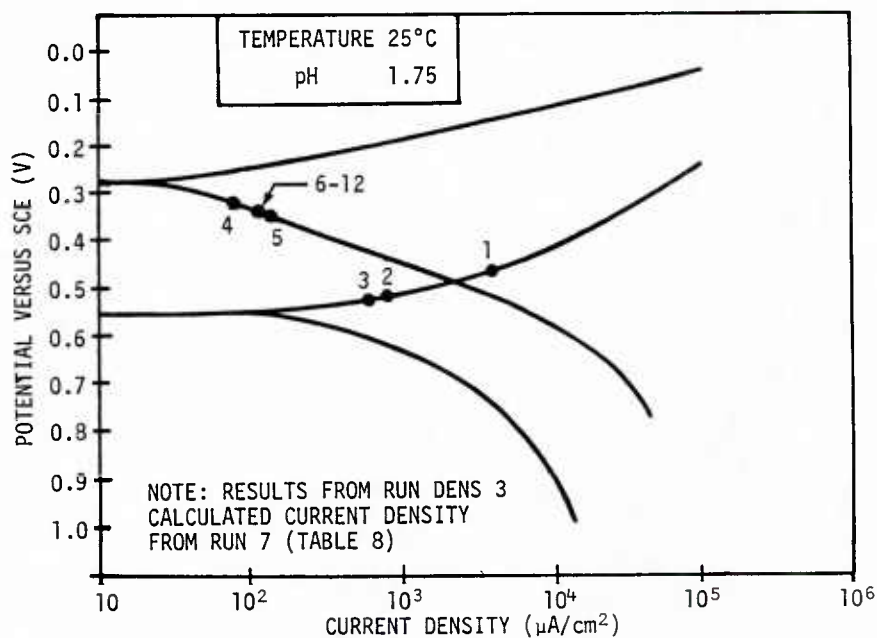


Figure 24. Anodic and Cathodic Normal Current Density Values as a Function of Radial Position

A - ANODIC SURFACE
 C - CATHODIC SURFACE
 E - ELECTROLYTE
 σ - CONDUCTIVITY
 t - TIME

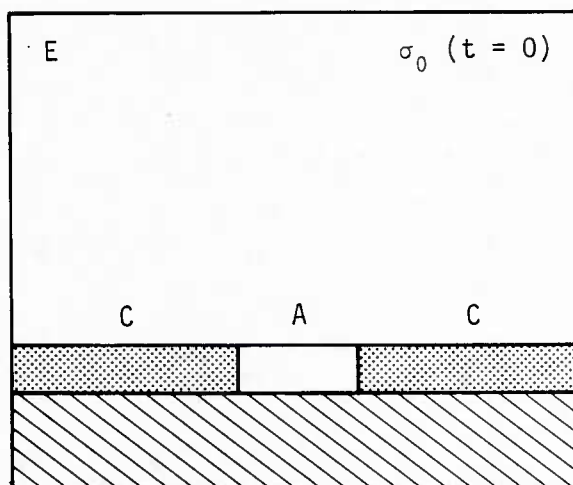


Figure 25a. Simple Anodic/Cathodic Geometry
 Electrolytic Conductivity Constant

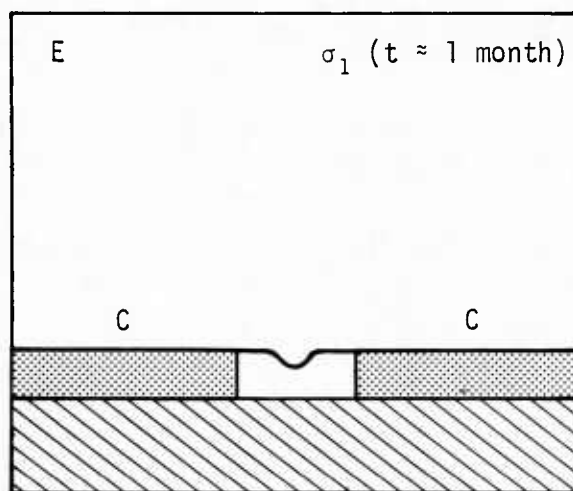


Figure 25b. Complex Anodic/Cathodic Geometry Updated Electrolytic
 Conductivity, Anodic Loss Due to Faraday's Law

Figure 25. Anodic Loss Based on Faraday's Law and
 Finite-Element Current Density Predictions

REFERENCES

1. N. D. Greene and M. G. Fontana, "A Critical Analysis of Pitting Corrosion," Corrosion, vol. 15, no. 32, 1959, p. 41.
2. J. A. M. Kolotyrkin, "Pitting Corrosion of Metals," Corrosion, vol. 19, no. 8, 1963, p. 261t.
3. W. D. France, Jr., and N. D. Greene, "Comparison of Chemically and Electrolytically Induced Pitting Corrosion," Corrosion, vol. 26, no. 1, 1970, p. 1.
4. C. Wagner, Die Chemische Reaktion der Metalle Handbuch der Metallphysik J, Akademische Verlagsgesellschaft Becker und Erler Kom.-Ses., vol. 2, Leipzig, East Germany, 1940, p. 165.
5. K. J. Vetter, Electrochemical Kinetics, Theoretical and Experimental Aspects, Academic Press, Inc., NY, 1967, p. 745.
6. B. F. Brown, T. Kruger, and R. W. Staehle, Editors, Localized Corrosion, National Association of Corrosion Engineers, Houston, TX, 1974.
7. T. Okada and T. Hashino, "A Contribution to the Kinetic Theory of Pitting Corrosion," Corrosion Science, vol. 17, no. 5, 1977, p. 671.
8. R. Alkire and D. Siitari, "The Location of Cathodic Reaction During Localized Corrosion," Journal of the Electrochemical Society, vol. 126, no. 15, 1979.
9. E. McCafferty, "Distribution of Potential and Current in Circular Corrosion Cells Having Unequal Polarization Parameters," Journal of the Electrochemical Society, vol. 124, no. 12, 1977, p. 1869.
10. J. W. Fu, "IR Drop Corrosion in Electrochemical Corrosion Probes Using a Finite Element Calculation," CORROSION/81 - NACE Conference, Toronto, Canada, March 1981.
11. R. G. Kasper and M. G. April, "Electrogalvanic Finite Element Analysis of Partially Protected Marine Structures," CORROSION/82, Houston, TX, 22 to 26 March 1982.
12. R. S. Munn, "Numerical Analysis of Galvanic Systems for Marine Cathodic Protection System Design," CORROSION/82, Houston, TX, 22 to 26 March 1982.
13. H. P. E. Helle, G. H. M. Beek, and J. T. Ligtelign, "Numerical Determination of Potential Distributions and Current Densities in Multielectrode Systems," Corrosion, vol. 37, no. 9, 1981, p. 522.
14. R. G. Kasper, "Electrochemical Modeling of Three-Dimensional Painted/Unpainted Metal Surfaces Using Finite Element Theory," Corrosion Research Conference, CORROSION/81, Toronto, Canada, 6 April 1981.

15. C. R. Crowe, "Localized Corrosion Currents from Graphite/Aluminum and Welded SiC/Al Metal Matrix Composites," NRL Memorandum Report, Naval Research Laboratory, Washington, DC (in process).
16. R. G. Kasper and M. O. Duffy, Mathematical Models of Non-Linear Galvanic Polarization, NUSC Technical Report 6921, Naval Underwater Systems Center, New London, CT, 16 August 1983.
17. C. R. Crowe, "Localized Ionic Currents from a Corroding Iron-Copper Galvanic Couple," NRL Memorandum Report, Naval Research Laboratory, Washington, DC (in process).
18. R. G. Kasper and C. R. Crowe, "Calculated and Measured Current Densities in the Near-field of a Corroding Iron-Copper Galvanic Couple," (to be submitted to Journal of Electrochemistry).
19. Y. Ishikawa and H. S. Isaacs, The Study of Pitting Corrosion of Aluminum by Means of the Scanning Vibrating Electrode Techniques, Report No. BNL 33059, Brookhaven National Laboratory, Brookhaven, NY, 1983.

Appendix A

DATA FROM GALVANIC CORROSION EXPERIMENTS

Parameters for the galvanic corrosion experiments were as follows:

Beaker diameter, 8.8 cm;

Beaker height, approximately 1.5 cm;

Electrolyte height, 0.95 cm;

Anode diameter (pure iron), 0.635 cm;

Cathode diameter (pure copper), 5.05 cm;

Electrolyte impedance, 16 Ω /cm; and sigma = 6.25 mhos/m;

Tests were run by Dr. C. R. Crowe, Code 6372, Naval Research Laboratory, Washington, DC 20375, at Brookhaven National Laboratory, in collaboration with Dr. H. Isaacs.

Measured normal current-density values for Runs 15 and 18 are given in table A-1 as a function of radial distance.

Table A-1. Measured Normal Current-Density Values as a Function of Radial Distance, August 1983, Runs 15 and 18

R (mm)	J_z ($\mu\text{A}/\text{cm}^2$)	
	Run 15, $Z = 650 \mu\text{m}$ $0.0 \text{ m} \leq R \leq 0.024 \text{ m}$	Run 18, $Z = 1150 \mu\text{m}$ $0.0 \text{ m} \leq R \leq 0.024 \text{ m}$
0	1135.78	954.0
1	1073.26	901.1
2	864.860	768.5
3	635.620	535.3
4	484.53	307.4
5	364.70	164.3
6	268.83	106.0
7	191.207	79.5
8	130.250	79.5
9	78.150	68.9
10	52.1	53.0
11	26.05	58.3
12	0.00	53.0
13	-8.336	53.0
14	-34.38	53.0
15	-26.05	53.0
16	-43.24	53.0
17	-43.24	53.0
18	-26.05	53.0
19	-26.05	53.0
20	-34.91	53.0
21	-26.05	53.0
22	-26.05	53.0
23	-26.05	58.3
24	-26.05	53.0

INITIAL DISTRIBUTION LIST

Addressee	No. of Copies
ONR, Code 431 (Dr. P. Clarkin)	3
NRL, Code 6314 (Dr. E. McCafferty), 6372 (Dr. C. R. Crowe), 6000, 6300, 2627)	5
Brookhaven National Laboratory (Dr. N. S. Isaacs)	1
NAVSEA, SEA-05R, -05R25 (H. Vandervelt), -05E1 (W. Strasburg)	3
Lehigh University (H. Leidheiser, R. P. Wei)	2
DWTNSRDC/ANNA (B. Bieberich, H. P. Hack, J. Scully, M. Farkas, Dr. B. Hood, G. Dadin)	6
DWTNSRDC/BETH, Code U31	1
APL, University of Washington (C. Sandwidth)	1
University of Delaware (S. C. Dexter)	1
Laque Center for Corrosion Technology (T. S. Lee)	1
Battelle Petroleum Technology Center (W. Boyd)	1
DTIC	12
Carnegie-Mellon University (I. M. Bernstein)	1
University of Illinois (H. K. Arnbaum)	1
NAVPGSCOL (Dr. D. H. E. ...)	1
Rensselaer Polytechnic Institute (J. Duquette)	1
Ohio State University (S. E. Wilde)	2
Rockwell International (Dr. P. Mansfield)	1
University of Pittsburgh (Pettit)	2
Martin Marietta Laboratories	1
Pennsylvania State University	1
Michigan State University (R. ...)	1
University of California at Los Angeles	1
Engineering & Applied Sciences	1
State University of New York	1
NAVAIRDEVCE (Dr. J. Deluccia)	1
NAVSURWEACTR (Library)	1
NOSC, Code 6565 (Library)	1
Naval Air Systems Command, Code 5304B	2
Naval Air Propulsion Test Center (Library)	1
Naval Construction Battalion	1
Naval Electronics Laboratory	1
Naval Missile Center	1
NAVWPNSCEN, Library	1
NASA, Lewis Research Center, Library	1
Naval Bureau of Standards, Washington, DC	3
Naval Facilities Engineering Command, Code 03	1
Commandant of the Marine Corps, Scientific Advisor, Code AX	1
Army Research Office	1
Army Materials and Mechanics Research Center	1
Air Force Office of Scientific Research/NE	1
NASA Headquarters, Washington, DC, Code RRM	1
Defense Metals and Ceramics Information Center	1
Oak Ridge National Laboratory	1
Los Alamos Scientific Laboratory, Report Librarian	1
Argonne National Laboratory	1
Brookhaven National Laboratory, Research Library	1
Lawrence Radiation Laboratory, Library	1

U217208

